The sensitivity of Southeast Pacific heat distribution to local and remote changes in ocean properties

Daniel C. Jones[1], Emma Boland[1], Andrew J.S. Meijers[1], Gael Forget[2], Simon A. Josey[3], Jean-Baptiste Sallee[4], and Emily Shuckburgh[1,5]

[1]British Antarctic Survey, Natural Environment Research Council, Cambridge, UK
[2]Massachusetts Institute of Technology, Cambridge, MA, USA
[3]National Oceanography Centre, Southampton, UK
[4]L'Ocean, CNRS, UPMC, Paris, France
[5]University of Cambridge, UK

Key Points:

- We define the recently ventilated Pacific (RVP) using numerical passive tracer distributions
- We use an adjoint model to calculate sensitivities of fixed-volume RVP to state anomalies
- Southeast Pacific heat distribution is most sensitive to basin-scale, mid-latitude changes

Corresponding author: D.C. Jones, `dannes@bas.ac.uk`

Abstract

The SO features ventilation pathways that transport heat and carbon from the surface ocean to the interior thermocline on timescales of decades to centuries, but the factors that control the distribution of heat along these pathways are not well understood. In this study, we use an observationally-constrained, physically consistent global ocean model to examine the sensitivity of the recently ventilated interior Pacific (RVP) sector of the Southern Ocean to changes in ocean temperature and salinity. First, we define the RVP using numerical passive tracer release experiments. We initialize numerical passive tracers in regions of weak stratification and deep mixed layers and allow them to circulate for 10 years; the resulting tracer distributions highlight the ventilation pathways into the interior thermocline. We use an ensemble of adjoint sensitivity experiments to quantify the sensitivity of the RVP heat content to changes in ocean temperature and salinity, decomposed into changes at constant density (i.e. kinematic sensitivities) and changes with varying density (i.e. dynamic sensitivities). We find that RVP heat content is most sensitive to ocean property changes in the South Pacific Gyre; RVP heat content is only weakly sensitive to ocean property changes in the high-latitude circumpolar circulation regime. Despite the localized nature of mode water subduction hotspots, changes in basin-scale density gradients are an important controlling factor on RVP heat content.

1 Introduction

The Southern Ocean (SO) is an important region for the uptake, storage, and transport of heat and carbon (Sabine et al., 2004; Sarmiento et al., 2004; Lenton & Matear, 2007; Ito et al., 2010; Talley, 2013; Roemmich et al., 2015). Over the period 1861-2005, the SO, defined as the ocean south of 30°S, is estimated to account for 43%±3% of anthropogenic carbon dioxide uptake and $75\% \pm 22\%$ of heat uptake, despite only occupying 30% of global surface ocean area (Frölicher et al., 2015). The SO's ability to absorb and transport this disproportionately high fraction of heat and carbon comes in part from a balance between powerful overlying westerly winds, strong buoyancy fluxes, and internal dynamics that maintains steeply tilted surfaces of constant density and localized pools of weakly stratified water (Russell et al., 2006). These pools of weakly stratified water, referred to collectively as Subantarctic Mode Water (SAMW), are refreshed by localized wintertime deep convection that occurs just north of the Antarctic Circumpolar Current (ACC) (Speer et al., 2000; Hanawa & Talley, 2001; Lumpkin & Speer, 2007; Talley, 2008; Herraiz-Borreguero & Rintoul, 2011; Speer & Forget, 2013). The processes of lateral induction, eddy-induced transport, and advection via the mean flow subduct the SAMW into the interior ocean at a rate that varies across interannual and decadal timescales (Karsten & Marshall, 2002; J.-B. Sallée et al., 2010; J. Sallée & Rintoul, 2011; J.-B. Sallée et al., 2012; Liu & Huang, 2012). Together with the denser and relatively fresher Antarctic Intermediate Water (AAIW), SAMW ventilates the subtropical thermocline on timescales of decades to centuries (Iudicone et al., 2007; J. Sallée et al., 2010; Cerovecki et al., 2013; Jones et al., 2016). Here, ventilation refers to the broad set of processes by which atmospheric and surface ocean properties are able to affect interior ocean properties. Ventilation is driven in part by the formation, subduction, and destruction of water masses and can be considered a consequence of the ocean's global overturning circulation (Marshall & Speer, 2012; Cerovečki & Mazloff, 2015).

Regional differences in subduction, ventilation, and the properties of the ventilated interior can impact (i.) the sequestration of anthropogenic heat and carbon into the interior thermocline and (ii.) the supply of nutrients to low latitudes via the overturning circulation (Sarmiento et al., 2004; Sabine et al., 2004; Khatiwala et al., 2009; Ito et al., 2010; Roemmich et al., 2015). The regionally specific nature of subduction and ventilation, and how those localized characteristics affect the distribution of heat, carbon, and nutrients in the ocean, is an active area of oceanographic study (Cerovecki et al., 2013; Jones et al., 2016). Despite these efforts, we still have relatively little knowledge on how regional variations in ocean state variables (e.g. temperature, salinity) and surface forcing can ultimately impact the properties of the ventilated interior. Advancements in this area may be especially helpful for improving projections of future ocean states, as changes in the Southern Ocean forcing-subduction-ventilation mechanism are expected to have a considerable impact on future climate (Cessi & Otheguy, 2003; Downes et al., 2009; Lovenduski & Ito, 2009; Morrison et al., 2011; J.-B. Sallée et al., 2012).

In order to quantify how regional variations in ocean state variables may affect the heat distribution in the ventilated interior ocean, we perform a set of adjoint sensitivity experiments using an observationally-constrained, physically consistent state estimate. First, we identify the recently ventilated interior ocean using a combination of physical state variables (e.g. potential vorticity, density, mixed layer depth) and numerical passive tracer distributions that track ventilation pathways from the surface into the interior. Our method for identifying the recently ventilated interior treats ventilation as a general process that may affect many different water masses, in contrast to approaches that consider one particular water mass (e.g. SAMW). We focus our attention on the Eastern Pacific because it features an especially efficient export pathway of water from the surface ocean into the interior thermocline, as measured by numerical passfive tracer experiments (Jones et al., 2016). For convenience, we refer to the recently ventilated interior Eastern Pacific as the RVP and the heat content of the RVP as RVPh. Although there is overlap between the two, we note that the RVP is more general than the region occupied by SAMW or any other particular water mass. Once we have identified the RVP, we perform a set of adjoint sensitivity experiments using, for consistency, the same numerical model setup that we used for the passive tracer experiments. Our adjoint model produces linear, time-evolving sensitivity maps, allowing us to identify locations and timescales where hypothetical anomalies could potentially impact the heat distribution in the ventilated interior, as revealed by the heat content of the fixed-volume RVP. Although we do not use this framework here, the sensitivity fields can roughly be interpreted as optimal linear perturbations, i.e. perturbations with the largest possible impact on RVPh, within the linear framework of the adjoint model (see a related but not identical example in Sévellec and Fedorov (2015)).

This paper is structured as follows: in section 2, we describe the ECCOv4 model setup, the design of our numerical tracer release experiments, and the design of our adjoint sensitivity experiments. In section 3, we examine the results of the tracer experiments in order to define the RVP, which is the control volume for our adjoint sensitivity experiments. In section 4, we examine the time-evolving sensitivities of RVPh to changes in temperature and salinity, decomposed into changes at constant density (i.e. kinematic sensitivities) and changes with varying density (i.e. dynamic sensitivities). We offer a brief summary with conclusions in section 5.

2 Methods

Here we describe the observationally-constrained global ocean model setup (section 2.1), the design of our numerical passive tracer experiments used to define the RVP (section 2.2), and the design of our adjoint sensitivity experiments (section 2.3).

2.1 Global ocean model setup

We use the modelling setup associated with ECCOv4 (release 2, hereafter ECCOv4-r2 or just ECCOv4). ECCOv4 is a *state estimate*, meaning that it has been adjusted to minimize the misfits between the model state and a suite of observations from various sources over the time period 1992-2011 (e.g. Argo float temperature and salinity profiles, ship hydrography, satellite altimetry). The model's initial conditions, surface forcing fields, and mixing parameters were iteratively adjusted in order to reduce model-data misfit. Because no artificial sources or sinks of heat were used in the ocean interior, ECCOv4 features closed budgets of heat, salt, and volume. The model setup is available for download on GitHub.com (`https://github.com/gaelforget/ECCOv4`) as an instance of the open source MIT general circulation model (MITgcm, `http://mitgcm.org/`, also available on GitHub). We briefly describe the relevant features of the ECCOv4 setup below; a more thorough description is available in Forget, Campin, et al. (2015) and references therein.

ECCOv4 is a global ocean model that uses a Lat-Lon-Cap (LLC) grid. Its horizontal grid size ranges from around 40-50 km at high latitudes up to roughly 110 km at the equator. It features parameterised diffusion, including both diapycnal and isopycnal components, simple convective adjustment, and the GGL mixed layer turbulence closure scheme (Gaspar et al., 1990). To represent the along-isopycnal effect of unresolved eddies, Forget, Campin, et al. (2015) used a bolus transport parameterization (Gent & Mcwilliams, 1990, hereafter GM). Although the horizontal resolution of ECCOv4 is relatively coarse (roughly 1°), its mixing properties are in good agreement with observations, thanks in part to the use of optimized, spatially-varying turbulent transport coefficients (Forget, Ferreira, & Liang, 2015). ECCOv4 features fully interactive dynamic sea ice, so that buoyancy and mass fluxes at the sea surface are recalculated based on the thermodynamic balance of Losch et al. (2010). Open ocean rain, evaporation, and runoff simply carry (advect through the free surface) the local SST and a salinity value of zero, and runoff is provided by a monthly climatology (Fekete et al., 2002). ECCOv4 calculates buoyancy, radiative, and mass fluxes using the bulk formulae of Large and Yeager (2009) with 6-hourly ERA-Interim re-analysis fields (Dee et al., 2011) as a "first guess" for the forcing fields. Specifically, we use wind stress, 2 m air temperature, 2 m specific humidity, wind speed, downward longwave radiation, and downward shortwave radiation as model inputs. These atmospheric state fields have been iteratively adjusted by the state estimation process in order to minimize model-data misfits. The ECCOv4-r2 setup that we use here does *not* use surface salinity restoring. For additional validation information, see the online supporting information and Forget, Campin, et al. (2015).

2.2 Design of the numerical passive tracer release experiments

Generally, on a selected timescale (e.g. 1 year, 10 years), we can consider the volume of the ocean that has been affected by near-surface properties (e.g. the temperature and salinity characteristics of the mode water formation regions) as having been ventilated via advection, diffusion, and mixing. In terms of an operational definition, the ventilated interior ocean can be identified using physical state variables, tracer distributions, or a combination of the two. Luyten et al. (1983) showed that, in a simple analytical model, pathways of potential vorticity (PV) can be used to separate the ventilated thermocline from the unventilated thermocline and also to separate regions of weak stratification from regions of strong stratification. This result helps justify the use of potential vorticity as a "dynamical tracer" that indicates thermocline ventilation pathways. Alternatively, one can derive ventilation pathways using the observed distributions of tracers such as tritium, helium-3 and chlorofluorocarbons, which are carried into the interior by both advection along ventilation pathways and by isopycnal and diapycnal mixing (Musgrave, 1990; Speer & Tziperman, 1992; Primeau & Holzer, 2006). In the interior, diapycnal mixing contributes to the erosion of water masses by homogenizing their properties across density surfaces (Trossman et al., 2012). In combination with PV and tracer considerations, the ventilated interior is generally considered to be located below the mixed layer, isolated from immediate contact with the surface.

We use a combination of physical state variables (e.g. PV, mixed layer depth, density) and numerical passive tracer release experiments to identify the recently ventilated interior ocean in ECCOv4. First, we initialize passive tracer in regions of weak stratification and deep mixed layers. More specifically, we calculate PV as $\log_{10}\left|f\rho_0^{-1}d\rho/dz\right|$, where $f = 2\Omega\sin(\phi)$ is the Coriolis parameter and ρ_0 is the reference density. For each release year, we calculate the August-September-October mean mixed layer depth, defined using a criteria based on the density change associated with a temperature variation $\Delta T = 0.8°\text{C}$ ((Kara et al., 2000)), and the minimum PV at the base of this mixed layer. We use a combination of the minimum PV threshold and a mixed layer depth contour to create the mixed layer masks as shown in Figure 1a. Within the mixed layer masks, we initialize the tracer from the surface down to the maximum mixed layer depth for the associated release year. All releases start on 1 January; our method of initializing tracer above the maximum mixed layer for the release year ensures that variation associated with seasonal release timings are minimal. We integrate the tracer equations in "online" mode for 10 years, i.e. we explicitly solve the momentum, buoyancy, and tracer equations at the same time. Note that although the bulk of the tracer used to define the RVP originates in the Pacific, a smaller fraction also comes from the Indian sector. The 10-year integration timescale allows a large fraction of weakly stratified water to subduct into the interior (Jones et al., 2016), and using a 10-year timescale allows us to carry out a suite of passive tracer and adjoint sensitivity runs within the 20-year observationally-constrained time period of ECCOv4. We then use the time-integrated tracer distribution to map out the ventilation pathways.

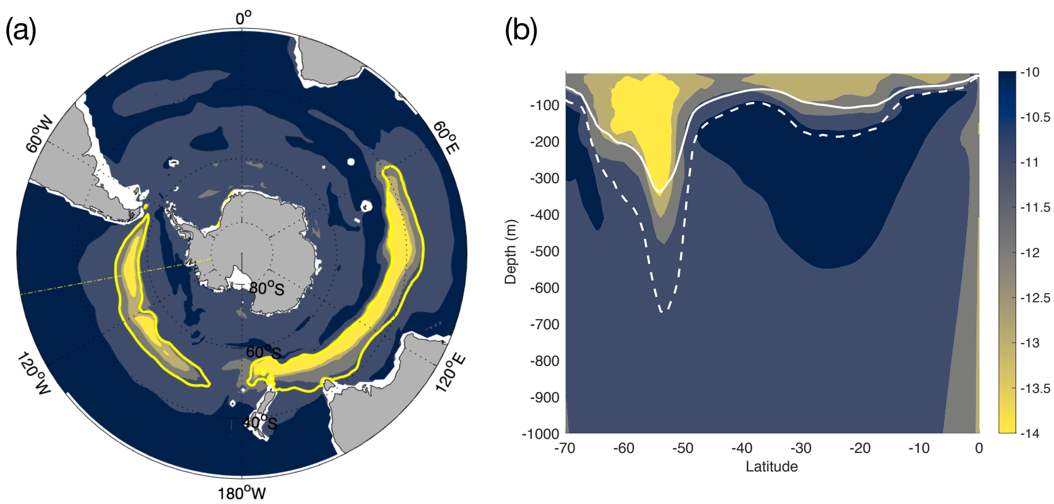

Figure 1. Selecting tracer release areas. Shown are ensemble median values of annual minimum potential vorticity across the years 1992-2011, on a logarithmic scale as (a) a cut through z=300 m. The yellow contour indicates a cut through the ensemble median mixed layer mask at z=300 m depth, and the yellow dot-dash line indicates the location of the cut in panel (b). (b) Section of ensemble median values of annual minimum PV across the years 1992-2011 at $100.5°W$, with ensemble median values for the annual mean (solid white line) and ASO mean (dashed white line) mixed layer depths.

2.3 Design of the adjoint sensitivity experiments

An adjoint model is a tool for sensitivity analysis; all other applications derive from there (Errico, 1997). Adjoint methods can be used to construct state estimates (e.g. the ECCOv4 state estimate used in this paper) via the iterative optimization of model initial conditions, model parameters, and surface forcing (collectively called the "controls"), guided by *gradients* or *sensitivities* that are calculated by an adjoint model. In such applications, the sensitivities indicate how one needs to adjust the controls in order to reduce the *cost function*, which is a measure of model-data misfit over the duration of the model run. This method enables objective, physically consistent, and efficient model optimization that would otherwise require considerable ad-hoc parameter tuning and/or the introduction of artificial sources or sinks of heat and salt into the interior.

More generally, adjoint methods also enable us to carry out efficient and comprehensive sensitivity studies, such as the one presented in this manuscript. In a traditional "forward" perturbation experiment, the experimenter introduces a perturbation into the model (e.g. a change in the initial temperature pattern) and examines the effect on some quantity of interest (e.g. RVPh). Using this method, the experimenter cannot feasibly determine if the perturbation they selected is the ideal or optimal one (i.e. the one with the largest effect on RVPh) without performing a very large number of numerical experiments. By contrast, in an adjoint sensitivity experiment, one selects a quantity of interest (e.g. annual mean RVPh) and uses an adjoint approach to calculate *gradients* or *sensitivities*. The sensitivity fields indicate the linear perturbations with the largest possible impact on RVPh. For examples of adjoint sensitivity experiments, see Verdy et al. (2014); Sévellec and Fedorov (2015); Jones et al. (2018), and many others. We refer the reader to these works for a more thorough and general description to adjoint modeling (Thacker & Long, 1988; Marotzke et al., 1999; Heimbach, 2008; Mazloff et al., 2010; Griewank & Walther, 2012; Verdy et al., 2014; Forget, Campin, et al., 2015; Fukumori et al., 2015; Jones et al., 2018, for example).

We perform a set of such adjoint sensitivity experiments in order to examine the sensitivity of RVPh to interior ocean properties. The objective function is defined as the annual- and volume-mean RVPh:

$$\tilde{J} = \frac{1}{V\Delta t}\int_V \int_{\Delta t} \rho_0 c_p \theta(\mathbf{r}, t) dt dV, \tag{1}$$

where ρ_0 is the reference density, c_p is the heat capacity of seawater, θ is the potential temperature, $\mathbf{r}$ is the position vector, t is the time, V is the control volume, and Δt is the time period of the integration. For convenience, we scale $\tilde{J}$ by the constant $\rho_0 c_p$, so RVPh= $J = \tilde{J}/\rho_0 c_p$, meaning that RVPh has units of $^\circ C$.

We compute an ensemble of six adjoint sensitivity experiments, with the objective function defined over the last year of each run, i.e. from 1 January to 31 December, with objective function years ranging from 2006 through 2011. Each experiment spans a minimum of 15 years, up to a maximum of 20 years. We allow the RVP to vary by ensemble member based on the results of the passive tracer experiments. Our ECCOv4 adjoint model calculates the sensitivities of these objective functions to a set of independent variables, including temperature ($\partial J/\partial T$) and salinity ($\partial J/\partial S$); the sensitivity fields vary with space (latitude, longitude, depth) and time. We use 14-day averaged sensitivity fields throughout.

3 Identifying the recently ventilated interior ocean

We use a six-member ensemble of passive tracer experiments with release years ranging from 1996 to 2001 to identify the RVP in ECCOv4. The ensemble mean, 10-year integrated tracer histogram (Figure 2 and Movie S1) highlights the ventilation pathways from the Southern Ocean mixed layer into the interior thermocline. In order to focus on the fraction of the tracer that is well isolated from the surface after subduction, we discard tracer above the 1992-2011 maximum mixed layer depth. The time-integrated, normalized tracer distribution covers roughly the top 1000 m of the Southern Hemispheric model domain. The overall tracer distribution can be used to examine regional variations in the ventilation process.

The normalized tracer distribution features several cores, i.e. local maxima with some degree of spatial coherence across latitudes and longitudes. In the Atlantic sector, we find a core below the 1992-2011 maximum MLD in the subtropical latitudes (roughly between 30°S-10°S) that drifts southwards before merging with a broad pattern that stretches from the Weddell Sea, across the ACC, and into the subtropics. The approximately zonal Atlantic distribution bears the imprint of the convergence of the Brazil current and the ACC. In the Indian sector, the tracer distribution is influenced by the Agulhas current and the broader circulation of the South Indian Gyre that is characterized by relatively

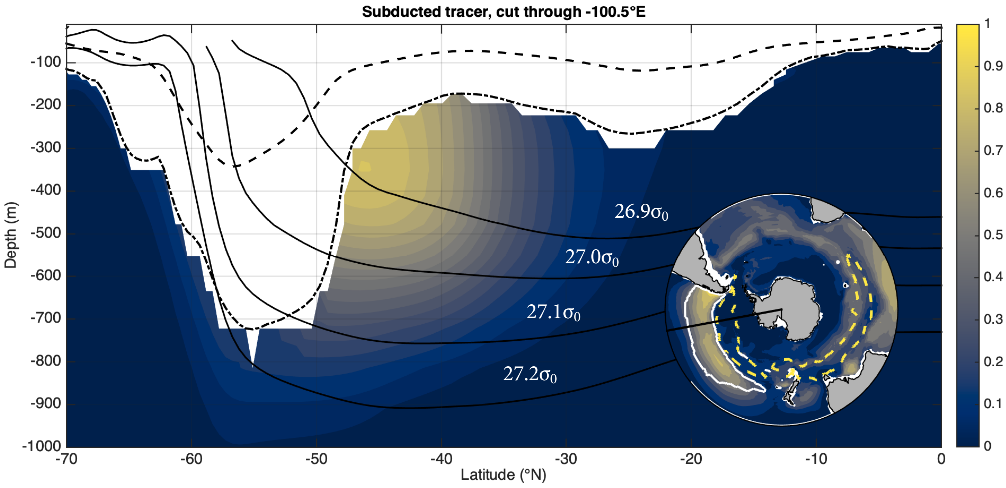

Figure 2. Defining the recently ventilated interior. Shading indicates the ensemble mean time-integrated tracer over the entire 10 year length of the numerical simulations. Values have been normalized by the maximum value. Also shown is the mean mixed layer depth (dashed lines) and maximum mixed layer depth (dash-dot lines) over the length of the 10 year simulation. Solid lines indicate potential density surfaces. Tracer above the maximum mixed layer has been discarded. Although we discard the tracer lighter than $26.9\sigma_0$ when defining the RVP, we kept this tracer in the figure for visualization purposes. Inset figure is the column-integrated tracer histogram, which is normalized by the maximum column-integrated value, after discarding the tracer above the maximum mixed layer, along with a cut through the ensemble median mixed layer mask at z=300 depth (yellow dashed contours) and a cut through the ensemble median ventilated water mask at z=553 m (white solid contour).

shallow overturning in density space; here, we find the core of the distribution at roughly 500 m and densities lighter than the $26.9\sigma_0$ density surface. In the Pacific sector, we find relatively large values throughout the entire South Pacific Gyre (SPG), with two distinct cores. The core of the distribution in the western SPG is found at densities lighter than $26.9\sigma_0$ and is affected by tracer that subducts in the Indian sector, whereas the core of the distribution in the eastern SPG largely straddles the $26.9\sigma_0$ line and is relatively less affected by tracer that subducts in the Indian sector. High tracer concentrations in the eastern region of the SPG highlights the relatively efficient Eastern Pacific export pathway that was previously identified in high-resolution simulations (Jones et al., 2016, Figure 8d).

In order to define the RVP, we use the 10-year integrated tracer concentrations and some additional physical and geographical criteria, selecting grid cells that satisfy the following four conditions:

- be located below the maximum mixed layer over the entire ECCOv4-r2 period (i.e. 1992-2011)
- time-integrated tracer concentration is at least 10% of the global ocean maximum value
- be located in the Southeast Pacific, between 170°W-60°W and 60°S-20°S
- potential density is greater than or equal to $26.9\sigma_0$

The $26.9\sigma_0$ surface delineates lighter waters from waters that are at least as dense as the SAMW. The resulting RVP for any given release year is a three-dimensional volume with a lateral imprint that varies with depth (Figure 3 and Figure S5). Between roughly 300-500m (Figure 3(a)-(c)), the areal extent of the RVP changes with depth and sits largely in the Southeast Pacific, north of the regions with deep mixed layers. The structure of the RVP at these depths reflects the subduction and ventilation pattern associated with the Eastern Pacific export pathway (Jones et al., 2016). Between roughly 500-700 m (Figure 3(d)-(e)), the RVP reaches its maximum areal extent, covering a large fraction of the SPG.

3.0.1 The RVP is more general than SAMW

Although the RVP has considerable overlap with the density ranges associated with SAMW, it is more general than SAMW alone. Our passive tracers ventilate a wide range of water masses, including SAMW, AAIW, and the lightest part of the Circumpolar Deep Water (CDW). In this way, our RVP approach is broader than an approach focused on a particular density range, in that it allows us to consider a wider range of ventilated water mass types than SAMW alone. Because RVPh is the heat content of a fixed volume, RVPh is a measure of the heat distribution in the target region, as RVPh may be affected by both isopycnal heave and by changes in properties along isopycnals. RVPh may have different sensitivities than the SAMW heat content, which may be affected by changes in the volume of SAMW and/or changes in the properties of water in the SAMW density range. We briefly explore this distinction in the discussion section of our companion paper.

Having defined the RVP in ECCOv4, we can now perform a set of adjoint sensitivity experiments using the adjoint capability of the ECCOv4 model setup.

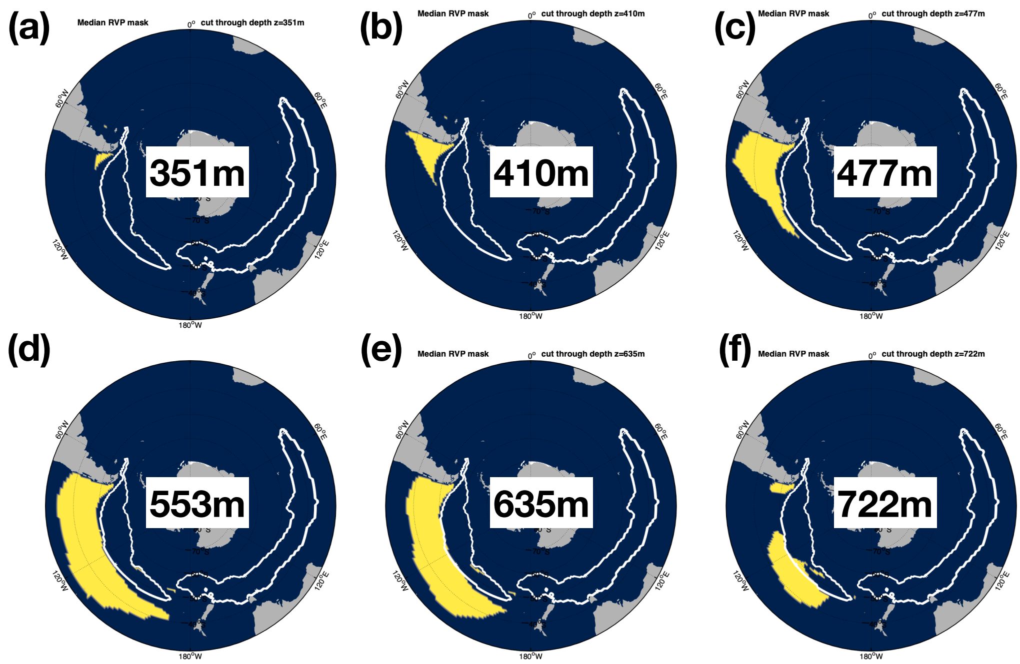

Figure 3. Vertical structure of the ensemble median RVP. Yellow regions are included in the RVP. A cut through the ensemble median mixed layer mask at roughly 300 m is shown for reference (white solid contours).

4 Sensitivities of interior heat content to local and remote anomalies

Here we examine the sensitivity of RVPh to changes in temperature and salinity, decomposed into changes at constant density (i.e. kinematic sensitivities) and changes with varying density (i.e. dynamic sensitivities). In section 4.1, we show how sensitivities to temperature and salinity perturbations can be cast in terms of kinematic and dynamic sensitivities. In section 4.2, we investigate the spatial and temporal structure of the kinematic sensitivities, focusing on both the interior and the surface. Finally, in section 4.3, we examine the spatial and temporal structure of the dynamic sensitivities, including regional patterns in the interior and at the surface. In this analysis, we use the time-variable -0.25 m ECCOv4 SSH contour as a proxy for the Subantarctic Front (SAF) that roughly divides the Southern Ocean into two regions - one dominated by gyre-like circulation and another region dominated by the circumpolar flow associated with the ACC (Kim & Orsi, 2014).

4.1 Defining kinematic and dynamic sensitivities

Following Marotzke et al. (1999) and Jones et al. (2018), we decompose the adjoint sensitivity fields into sensitivities to changes that propagate along isopycnals (i.e. kinematic) and sensitivities to changes in density (i.e. dynamic). Writing the objective function in terms of density and temperature $J = J[\rho(T,S),T]$ allows us to write the sensitivities as follows:

$$\left(\frac{\partial J}{\partial T}\right)_S = \left(\frac{\partial J}{\partial \rho}\right)_T \left(\frac{\partial \rho}{\partial T}\right)_S + \left(\frac{\partial J}{\partial T}\right)_\rho . \tag{2}$$

The first term on the right-hand side of equation 2 is the "dynamic" component of the sensitivity (i.e. sensitivity to changes in density), and the second term on the right-hand side is the "kinematic" component (i.e. dynamically-inactive sensitivities to temperature anomalies). Using the coefficient of thermal expansion α and coefficient of haline contraction β, defined as

$$\alpha \equiv -\frac{1}{\rho}\left(\frac{\partial \rho}{\partial T}\right)_S \text{ and } \beta \equiv \frac{1}{\rho}\left(\frac{\partial \rho}{\partial S}\right)_T , \tag{3}$$

we can write

$$\left(\frac{\partial J}{\partial S}\right)_T = \left(\frac{\partial J}{\partial \rho}\right)_T \left(\frac{\partial \rho}{\partial S}\right)_T = \beta\rho\left(\frac{\partial J}{\partial \rho}\right)_T , \tag{4}$$

and the dynamic sensitivity becomes:

$$F_{dyn} = \left(\frac{\partial J}{\partial \rho}\right)_T \left(\frac{\partial \rho}{\partial T}\right)_S = \frac{1}{\beta\rho}\left(\frac{\partial J}{\partial S}\right)_T \left(\frac{\partial \rho}{\partial T}\right)_S = -\frac{\alpha}{\beta}\left(\frac{\partial J}{\partial S}\right)_T . \tag{5}$$

We can write the kinematic sensitivity as:

$$F_{kin} = \left(\frac{\partial J}{\partial T}\right)_S + \frac{\alpha}{\beta}\left(\frac{\partial J}{\partial S}\right)_T . \tag{6}$$

Physically, kinematic sensitivities indicate the linear response of the objective function to the simultaneous application of a small temperature change and a compensating salinity change of the form $\Delta S = \Delta T\alpha/\beta$, such that density remains constant following the linearized equation of state for seawater, $\rho = \rho_0(1 - \alpha\Delta T + \beta\Delta S)$. We can refer to these perturbations as "density-compensated temperature anomalies". In contrast, dynamic sensitivities indicate the linear response of the objective function to the application of a temperature change ΔT or a density-equivalent salinity change of $\Delta S = -\Delta T\alpha/\beta$ in the equation of state. The linear response is given by $\Delta J = F_{dyn}\Delta T = F_{dyn}(-\Delta S\beta/\alpha)$.

We use 14-day averaged, three-dimensional α/β fields derived from ECCOv4-r2 potential temperatures and salinities using the TEOS-10 toolbox (McDougall & Barker, 2011). Next, we examine the kinematic and dynamic sensitivities of RVPh.

4.2 Sensitivity to changes at constant density

Kinematic sensitivity fields approximately indicate potential source water pathways. More specifically, one can think of the kinematic sensitivity fields as indicating the eventual response of annual mean RVP heat content to a spatially uniform, density-compensated potential temperature perturbation that is sustained for some time (in our case, two weeks) and allowed to propagate. Regions with zero sensitivity cannot affect RVPh; such regions are not connected to the RVP via advection and mixing on the associated timescales. The kinematic sensitivity fields are positive or zero nearly everywhere; an increase/decrease in temperature in regions with non-zero sensitivities eventually increases/decreases RVP heat content on the indicated lag timescale (Figure 4).

The near-surface kinematic sensitivity fields highlight the potential propagation pathways of anomalies into the SAMW formation regions, where they can be subducted below the mixed layer and exported into the thermocline (Figure 4, left column). The largest near-surface sensitivity fields tend to be found just north of the SAF proxy, within or upstream of regions of deep mixed layers and mostly south of the RVP areal extent. Density-compensated anomalies cannot typically propagate from directly above the RVP into the RVP itself on the timescales considered here; they are not typically advected into the regions of deep mixing. On timescales longer than 10 years, the near-surface sensitivities extend across the entire Southern Ocean, putting a lower bound on the temperature anomaly propagation timescale from the Atlantic to the RVP (Figure 4, left column). On timescales longer than roughly 5-6 years, we find sensitivities south of the SAF proxy in the Indian basin; here wind stress may advect anomalies across the SAF via Ekman transport. On shorter timescales, the sensitivity fields are more localized around the southeast Pacific mixed layer region and are typically smaller in magnitude. Temperature anomalies can only affect RVPh if they have sufficient time to propagate into the mixed layer, subduct, and get exported; only very local, targeted anomalies can affect RVPh on timescales shorter than 1-2 years. The persistent local maximum in the southeast Pacific indicates a relatively rapid route from the surface into the RVP. The near-surface sensitivity fields display a clear seasonal cycle, peaking in late August in the East Pacific and early August in the West Pacific and Indian basins, during the strong mixing phase that occurs as the mixed layer deepens before reaching its maximum depth in mid-September (Figure 5g and Movie MS02).

The interior sensitivity fields highlight the long residence time of local hypothetical perturbations in the interior of the gyre, as well as the pathways of interior ocean advection into the RVP (Figure 4, right column and Movie MS03). We find non-zero sensitivities to hypothetical anomalies within the RVP throughout the entire 16-year adjoint sensitivity experiment, indicating that RVPh is sensitive to local density-compensated temperature anomalies on timescales of at least 16 years. The spatially-integrated local sensitivity time series is well-described by a two-term exponential with decay rates of 1.23 years and 7.63 years (Figure 5(b)). Outside of the RVP, we mostly find non-zero sensitivities north of the SAF proxy in all three ocean basins; Ekman transport cannot directly advect anomalies across the SAF proxy at this depth (Figure 5(e,f)). The sensitivity fields spread westward with timescale, reflecting the advective timescale between basins (Figure 5(h)). In a spatially-integrated sense, these non-local sensitivities outside of the RVP exceed the spatially-integrated local sensitivities within the RVP on timescales longer than roughly 1.6 years (Figure 5(b)). On timescales longer than 10 years, we find sensitivities extending along the East Australian Current and, in contrast with the surface sensitivities, sensitivities along the Agulhas Current and associated retroflection as well. Surface anomalies in the Agulhas Current cannot affect RVPh on the timescales considered here, but anomalies in the interior (here, roughly 550 m) can eventually alter RVPh. We also find some sensitivity at this depth extending along the Brazil current. Notably, the Agulhas current is the only major Southern Hemispheric western boundary current with zero kinematic sensitivity in the near-surface and non-zero kinematic sensitivity in the interior (Movies MS01 and MS02). In terms of spatially integrated sensitivities, the West Pacific value exceeds the East Pacific value on timescales longer than throughly 3 years.

The globally-integrated kinematic sensitivity decreases with timescale, partly reflecting the tendency of air-sea exchange, represented in ECCOv4 as bulk formulae with a prescribed set of atmospheric variables, to dampen potential temperature anomalies (Figure 5(a)). The linear drop in sensitivity between lag 0 and lag 1 yr reflects the one-year integration period over which the objective function is calculated. There is no sensitivity to anomalies after year 1, after the integration has finished. Spatially-integrated sensitivities within the MLD mask peak at lag -7.2 yr (Figure 5(c)), and the sensitivities within the shallower regions decreases with timescale as a two-term exponential with decay constants of 8 yr and 34 yr. This is partly due to the fact that sensitivities exist below the surface, e.g. in the RVP itself, where the overlying mixed layers are typically shallow.

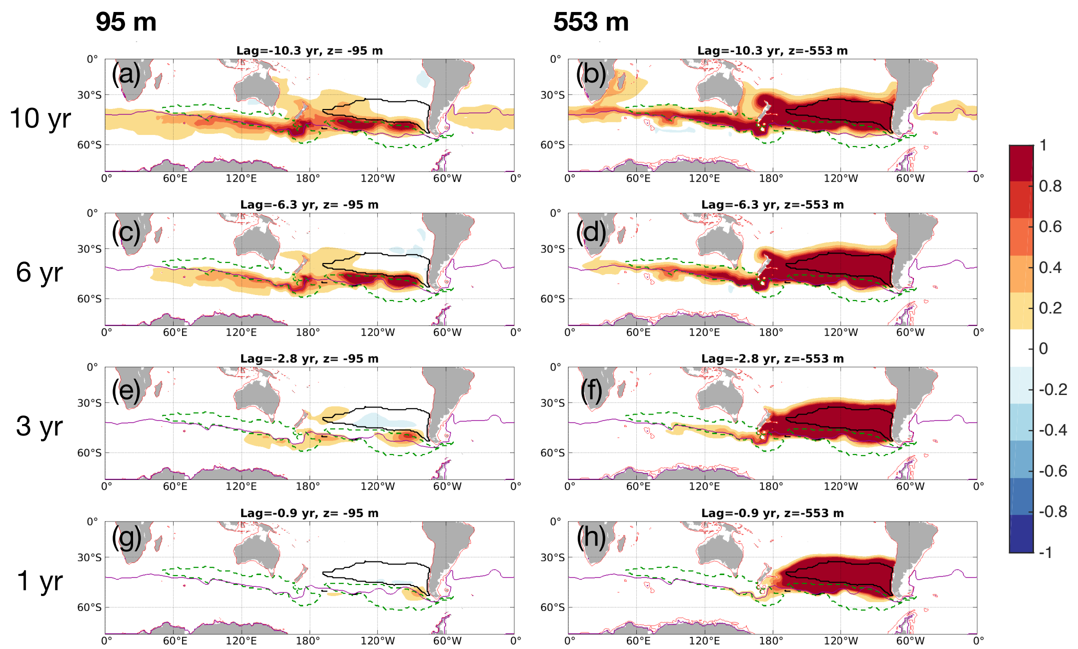

Figure 4. Relative ensemble mean sensitivities of RVPh to density-compensated temperature anomalies (i.e. kinematic sensitivities). Also shown is a cut through the RVP at roughly 553 m depth (black solid line), a cut through the mixed layer mask at roughly 300 m depth (green dashed line), and the SAF proxy (blue solid line). All fields have been scaled by the grid cell thickness Δz to allow for comparison between different depth levels. The plots have been further scaled by the global maximum sensitivity.

4.3 Sensitivity to changes in density

The dynamic sensitivity fields indicate patterns of density change that can alter RVPh, potentially by inducing changes isopycnal tilt and thereby affecting the associated transport and heat convergence into the RVP. More specifically, one can think of the dynamic sensitivity fields as indicating the eventual response of annual mean RVP heat content to a spatially uniform potential temperature perturbation, or a density-equivalent salinity perturbation, that is sustained for some time (two weeks, as with the kinematic

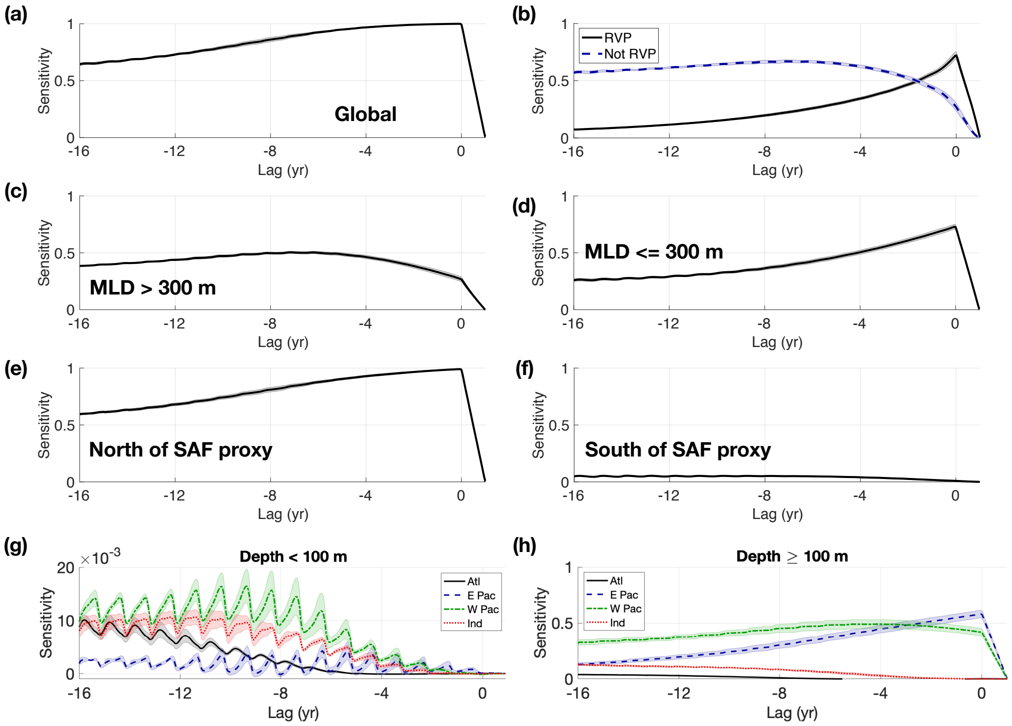

Figure 5. Relative kinematic sensitivities integrated over different volumes, indicating propagation timescales and relative magnitudes. Lines indicate ensemble means, and shading indicates one standard deviation across the ensemble. All values have been scaled by the same maximum and can be compared relative to each other. Here RVP refers to the three-dimensional control volume, MLD refers to the 300 m mixed layer depth mask, which does not change with time. Note that the axes in panel (g) are different from the others. We chose 120°W as the dividing longitude between the East and West Pacific basin.

sensitivity case) and allowed to affect the oceanic density structure. Regions of zero sensitivity cannot affect RVPh; such regions are not dynamically connected to the RVP. The dynamic sensitivity fields are both positive and negative, with the dipoles highlighting regions where a change in isopycnal tilt will change the associated circulation and ultimately RVPh (Figure 6).

The near-surface dynamic sensitivity fields are mostly negative across all lags, with local exceptions south of Australia and in in the eastern tropical Pacific (Figure 6, left column and Movie MS04). Negative values indicate regions where a hypothetical temperature increase, which will decrease density, will ultimately decrease RVP heat content. Similarly, in these regions a hypothetical temperature decrease, which will increase density, will ultimately increase RVP heat content. It is important to note that, due to technical limitations, our adjoint sensitivity fields *do not* represent non-linear changes. They *do* reflect changes in circulation and diffusion. So the negative near-surface values may represent the fact that, even under fixed mixing conditions, relatively lighter water may not reach the depths of the RVP as readily as relatively denser water, where "relative" refers to the background ECCOv4 state around which the adjoint sensitivities are calculated. Alternatively, the negative near-surface values may represent a hypothetical decrease (increase) in RVP heat convergence induced by a surface decrease (increase) in density. The negative sign of the sensitivity fields indicate that the hypothetical change in RVPh will have the opposite sign from that of the hypothetical temperature anomaly. As with the kinematic sensitivity fields, on shorter timescales the dynamic sensitivities become increasingly localized to the southeastern edge of the RVP, near the southern tip of South America. The near-surface fields also display a seasonal cycle, with similar timings as the kinematic fields (Figure 7(g)).

In contrast with the near-surface kinematic sensitivity fields, the near-surface dynamic sensitivity fields feature a persistent negative local minimum along the western coast of South America (Figure 6, left column). Considered together with the small positive values in the eastern tropical Pacific, this dipole reflects a sensitivity to the across-shelf pressure gradient. Variations in the across-shelf pressure gradients are associated with changes in basin-scale pressure gradients and the associated basin-scale circulation, which can ultimately change heat convergence and thus heat content within a selected ocean volume (Fukumori et al., 2015; Jones et al., 2018; Hughes et al., 2018).

The interior dynamic sensitivity fields highlight the sensitivity of annual mean RVP heat content to basin-wide density contrasts, equivalently expressed as tilted basin-scale isopycnal surfaces (Figure 6, right column and Movie MS05). This basin-scale structure is associated with the circulation of the South Pacific Gyre, which is in part maintained by pressure gradients induced by wind stress curl. We find a persistent sensitivity dipole stretched across the RVP, with positive values to the east and negative values to the west. The positive values reach into the tropics and extend westward with timescale, across both the Pacific and Indian basins. To illustrate the structure of these fields, consider a hypothetical potential temperature anomaly characterized by warming to the east of the RVP and cooling to the west of the RVP, imposed on the model vertical level centered at 553 m (Figure 6(d)). The warming to the east would decrease density at 553 m and, based on the positive sign of the sensitivity field, ultimately contribute to an increase RVPh. The cooling to the west would increase density at 553 m and, based on the negative sign of the sensitivity field, it would also increase RVPh. The change in RVPh induced by any anomaly is the product of the sensitivity field and the imposed anomaly, i.e. $\Delta J = F_{dyn}\Delta T$. In this scenario, we have imposed isopycnal deepening to the east and isopycnal shoaling to the west. In the RVP, isopycnal surfaces at roughly 500-600 m tend to shoal from west to east, so our imposed perturbation alters isopycnal surfaces locally, ultimately changing transport and increasing heat convergence in the RVP (Jones et al., 2018).

The interior sensitivity fields also feature a persistent sensitivity along the western coast of South America (Figure 6, right column). In contrast to the near-surface fields, which are fairly consistently negative along the shelf, the along-shelf interior fields are positive to the north and negative to the south. The north-south sign contrast indicates a sensitivity to barotropic structure, whereas the surface-interior sign contrast highlights an overall sensitivity to baroclinic density structure above the continental shelf. In addition, the interior fields display characteristic fingerprints of baroclinic Rossby waves, as seen by eastward propagating positive anomalies at depth (Figure 6, right column and Movie MS05). As with the surface fields, on shorter timescales the interior dynamic sensitivities become increasingly localized, albeit with a different structure than the surface fields. The interior fields are localized around the edge of the RVP, indicating a sensitivity to density contrasts across the RVP that can alter fluxes across the boundary of the RVP, and the interior sensitivities are also localized along the western coast of South America, indicating a short-timescale sensitivity to density changes along the continental shelf.

In a globally-integrated sense, the positive and negative sensitivities have a small positive residual that increases with timescale (Figure 7(a)). Sensitivities outside of the RVP are dominated by positive values, but using the RVP as a boundary for spatial integration obscures the importance of dipole structures (Figure 7(b)). The dipole structure is evident when integrating sensitivities using the MLD mask (Figure 7(c,d)) and when integrating north and south of the SAF proxy (Figure 7(e,f)). For the interior fields, the dipole structure is especially evident when contrasting the East Pacific and the West Pacific time series (Figure 7(h)).

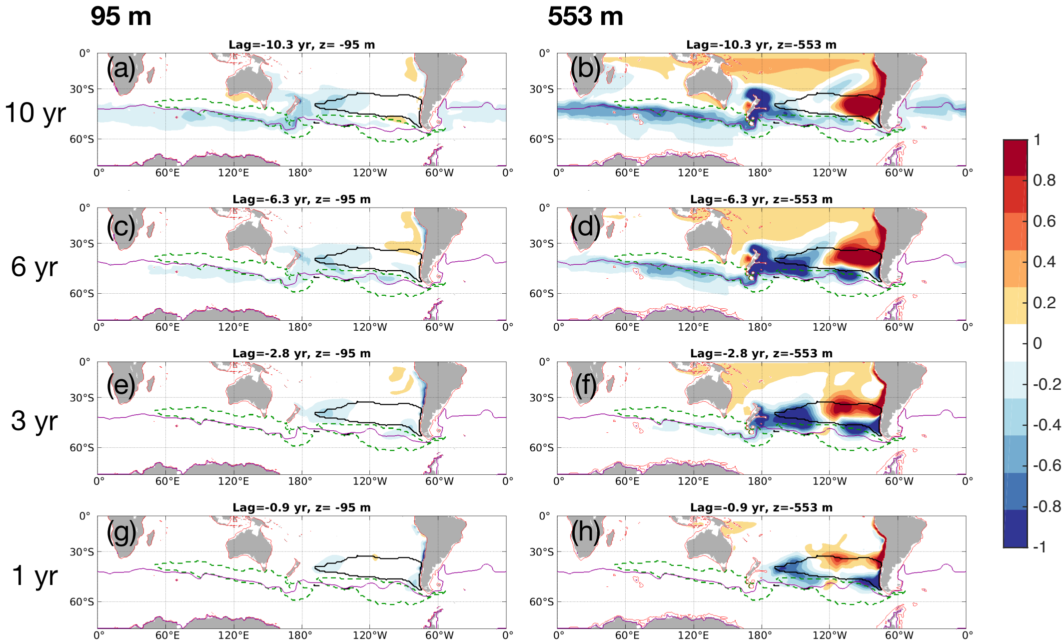

Figure 6. Relative ensemble mean sensitivities to changes in density (i.e. dynamic sensitivities). Scaling and units are the same as in Figure 4.

5 Summary and conclusions

Using an observationally-constrained state estimate, we used numerical passive tracer distributions and physical state variables (i.e. mixed layer depth, potential density, potential vorticity) to identify the recently ventilated Eastern Pacific sector of the Southern Ocean (RVP), which is a relatively efficient export pathway from the surface ocean into the interior thermocline. The RVP, defined on a 10-year timescale, is located north of the -0.25 m sea surface height contour (i.e. the SAF proxy) and north of the deep mixed layer regions, highlighting the ventilation pathway from the tip of South America, along the eastern Pacific boundary and out across the South Pacific Gyre in the interior. The RVP varies with depth, reaching maximum areal extent between 500-600 m, and it features some variation with tracer release year, mostly in its western extent (Figure S5).

Overall, the kinematic and dynamic fields suggest that the circulation of the South Pacific Gyre exerts a dominant influence on RVPh, and therefore on the distribution of heat in the Southeast Pacific. The sensitivity patterns are dominated by local effects within the RVP and basin-scale gradients, with upstream circumpolar effects playing a minor role. In both the kinematic and dynamic sensitivity fields, for lags longer than roughly

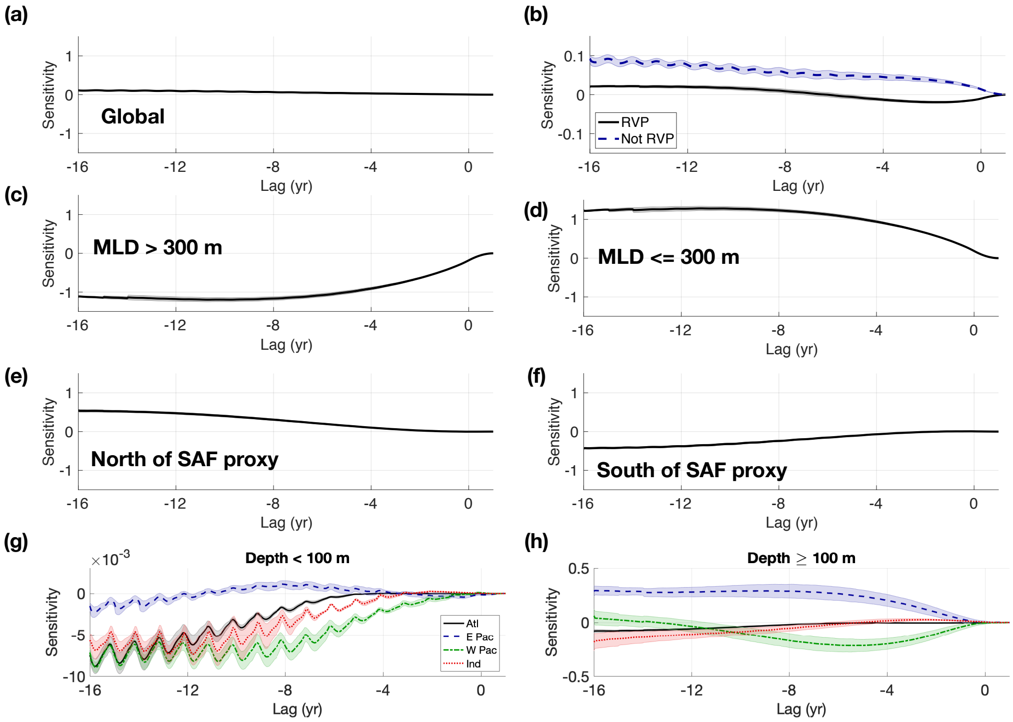

Figure 7. Relative dynamic sensitivities integrated over different volumes produce time series. Lines indicate ensemble means, and shading indicates one standard deviation across the ensemble. All values have been scaled by the same maximum and can be compared relative to each other. Note that the vertical scaling of panels b, g, and h differ from the others.

5-6 years, we find only weak sensitivities south of the SAF proxy, indicating that the heat content of the recently ventilated Eastern Pacific is not especially sensitive to high-latitude processes on timescales shorter than roughly 10-15 years.

By the end of the 21st century, Southern Ocean wind stress is expected to strengthen in magnitude and move poleward, resulting in a poleward shift of the gyres, and mixed layers are expected to shoal (Meijers, 2013). Our results suggest that the resulting subtropical, basin-scale temperature and salinity changes induced by the expected shifts in wind stress and heat flux may have a larger impact on the heat content of the ventilated Southeast Pacific, across the density ranges of the SAMW, AAIW, and the lightest CDW, than any ocean property changes at higher latitudes. In a companion manuscript, we examine the sensitivities of RVP heat content to changes in surface forcing.

Acronyms

ACC Antarctic Circumpolar Current

AAIW Antarctic Intermediate Water

CDW Circumpolar Deep Water

MLD Mixed layer depth

OLPs Optimal linear perturbations

RVP Recently ventilated Pacific sector of the Southern Ocean (fixed volume)

RVPh Heat content of the fixed-volume RVP

SAF Subantarctic Front

SAMW Subantarctic Mode Water

SO Southern Ocean

SPG South Pacific Gyre

SSH Sea surface height

Acknowledgments

This study is supported by grants from the Natural Environment Research Council (NERC), including [1] The North Atlantic Climate System Integrated Study (ACSIS) (grant NE/N018028/1, authors DJ, ES), [2] Securing Multidisciplinary UndeRstanding and Prediction of Hiatus and Surge events (SMURPHS) (grant NE/N006038/1, author EB), and [3] Ocean Regulation of Climate by Heat and Carbon Sequestration and Transports (ORCHESTRA) (grant NE/N018095/1, authors EB, AM). GF is supported by NASA award #6937342 and Simons Foundation award #549931. The ECCOv4-r2 model setup used in this work is available for download on Github (`https://github.com/gaelforget/ECCOv4`) as an instance of the MIT general circulation model (MITgcm, `http://mitgcm.org/`). Numerical model runs were carried out on ARCHER, the UK national HPC facility [`http://archer.ac.uk/`]. Adjoint code was generated using the TAF software tool, created and maintained by FastOpt GmbH [`http://www.fastopt.com/`].

References

Cerovečki, I., & Mazloff, M. (2015). The spatiotemporal structure of diabatic processes governing the evolution of Subantarctic Mode Water in the

Southern Ocean. *Journal of Physical Oceanography*, *46*, 683–710. doi: 10.1175/JPO-D-14-0243.1

Cerovecki, I., Talley, L. D., Mazloff, M. R., & Maze, G. (2013). Subantarctic Mode Water Formation, Destruction, and Export in the Eddy-Permitting Southern Ocean State Estimate. *Journal of Physical Oceanography*, *43*(7), 1485–1511. doi: 10.1175/jpo-d-12-0121.1

Cessi, P., & Otheguy, P. (2003). Oceanic teleconnections: Remote response to decadal wind forcing. *Journal of Physical Oceanography*, *33*(8), 1604–1617.

Dee, D. P., Uppala, S. M., Simmons, A. J., Berrisford, P., Poli, P., Kobayashi, S., ... Vitart, F. (2011). The ERA-Interim reanalysis: configuration and performance of the data assimilation system. *Quarterly Journal of the Royal Meteorological Society*, *137*(656), 553–597. doi: 10.1002/qj.828

Downes, S. M., Bindoff, N. L., Downes, S. M., Bindoff, N. L., & Rintoul, S. R. (2009). Impacts of Climate Change on the Subduction of Mode and Intermediate Water Masses in the Southern Ocean. *dx.doi.org*, *22*(12), 3289–3302 PB –. doi: 10.1175/2008JCLI2653.1

Errico, R. M. (1997). What Is an Adjoint Model? *Bulletin of the American Meteorological Society*, *78*(11), 2577–2591. doi: 10.1175/1520-0477(1997)078⟨2577:wiaam⟩2.0.co;2

Fekete, B. M., Vörösmarty, C. J., & Grabs, W. (2002). High-resolution fields of global runoff combining observed river discharge and simulated water balances. *Global Biogeochemical Cycles*, *16*(3), 15–1–15–10. doi: 10.1029/1999GB001254

Forget, G., Campin, J. M., Heimbach, P., Hill, C. N., Ponte, R. M., & Wunsch, C. (2015). ECCO version 4: an integrated framework for non-linear inverse modeling and global ocean state estimation. *Geoscientific Model Development*, *8*(10), 3071–3104. doi: 10.5194/gmd-8-3071-2015

Forget, G., Ferreira, D., & Liang, X. (2015). On the observability of turbulent transport rates by Argo: supporting evidence from an inversion experiment. *Ocean Science Discussions*, *12*(3), 1107–1143. doi: 10.5194/osd-12-1107-2015

Frölicher, T. L., Sarmiento, J. L., Paynter, D. J., Dunne, J. P., Krasting, J. P., & Winton, M. (2015). Dominance of the Southern Ocean in Anthropogenic Carbon and Heat Uptake in CMIP5 Models. *Journal of Climate*, *28*(2), 862–886.

doi: 10.1175/jcli-d-14-00117.1

Fukumori, I., Wang, O., Llovel, W., Fenty, I., & Forget, G. (2015). A near-uniform fluctuation of ocean bottom pressure and sea level across the deep ocean basins of the Arctic Ocean and the Nordic Seas. *Progress in Oceanography*, *134*(C), 152–172. doi: 10.1016/j.pocean.2015.01.013

Gaspar, P., Grégoris, Y., & Lefevre, J. M. (1990). A simple eddy kinetic energy model for simulations of the oceanic vertical mixing: Tests at station Papa and long-term upper ocean study site. *Journal of Geophysical Research: Atmospheres*, *95*(C9), 16179–16193. doi: 10.1029/JC095iC09p16179

Gent, P. R., & Mcwilliams, J. C. (1990). Isopycnal Mixing in Ocean Circulation Models. *Journal of Physical Oceanography*, *20*(1), 150–155. doi: 10.1175/1520-0485(1990)020⟨0150:imiocm⟩2.0.co;2

Griewank, A., & Walther, A. (2012). *Evaluating Derivatives* (Second ed.). Society for Industrial and Applied Mathematics. doi: 10.1137/1.9780898717761

Hanawa, K., & Talley, L. (2001). Mode Waters. In G. Siedler & J. Church (Eds.), *Ocean circulation and climate* (pp. 373–386). International Geophysics Series.

Heimbach, P. (2008). *The MITgcm/ECCO adjoint modelling infrastructure.* Clivar Exchanges.

Herraiz-Borreguero, L., & Rintoul, S. R. (2011). Subantarctic mode water: distribution and circulation. *Ocean Dynamics*, *61*(1), 103–126. doi: 10.1007/s10236-010-0352-9

Hughes, C. W., Williams, J., Blaker, A., Coward, A., & Stepanov, V. (2018). A window on the deep ocean: The special value of ocean bottom pressure for monitoring the large-scale, deep-ocean circulation. *Progress in Oceanography*, *161*, 19–46. doi: 10.1016/j.pocean.2018.01.011

Ito, T., Woloszyn, M., & Mazloff, M. (2010). Anthropogenic carbon dioxide transport in the Southern Ocean driven by Ekman flow. *Nature*, *463*, 80. doi: 10.1038/nature08687

Iudicone, D., Rodgers, K., Schopp, R., & Madec, G. (2007). An exchange window for the injection of Antarctic Intermediate Water into the South Pacific. *Journal of Physical Oceanography*, *37*, 31–49. doi: http://dx.doi.org/10.1175/JPO2985.1

Jones, D. C., Forget, G., Sinha, B., Josey, S. A., Boland, E. J. D., Meijers, A. J. S.,

& Shuckburgh, E. (2018). Local and Remote Influences on the Heat Content of the Labrador Sea: An Adjoint Sensitivity Study. *Journal of Geophysical Research - Oceans*, *105*(2-3), 182. doi: 10.1002/2018JC013774

Jones, D. C., Meijers, A. J. S., Shuckburgh, E., Sallée, J.-B., Haynes, P., McAufield, E. K., & Mazloff, M. R. (2016). How does Subantarctic Mode Water ventilate the Southern Hemisphere subtropics? *Journal of Geophysical Research - Oceans*, *121*(9), 6558–6582. doi: 10.1002/2016jc011680

Kara, A. B., Rochford, P. A., & Hurlburt, H. E. (2000). An optimal definition for ocean mixed layer depth. *Journal of Geophysical Research - Oceans*, *105*(C7), 16803–16821. doi: 10.1029/2000JC900072

Karsten, R., & Marshall, J. (2002). Testing theories of the vertical stratification of the ACC against observations. *Dynamics of Atmospheres and Oceans*, *36*, 233–246.

Khatiwala, S., Primeau, F., & Hall, T. (2009). Reconstruction of the history of anthropogenic CO2 concentrations in the ocean. *Nature*, *462*(7271), 346–349. doi: 10.1038/nature08526

Kim, Y. S., & Orsi, A. H. (2014). On the Variability of Antarctic Circumpolar Current Fronts Inferred from 1992–2011 Altimetry*. *Journal of Physical Oceanography*, *44*(12), 3054–3071. doi: 10.1175/JPO-D-13-0217.1

Large, W., & Yeager, S. (2009). The global climatology of an interannually varying air–sea flux data set. *Climate Dynamics*, *33*, 341–364. doi: 10.1007/s00382-008-0441-3

Lenton, A., & Matear, R. (2007). Role of the Southern Annular Mode (SAM) in Southern Ocean CO2 uptake. *Glob. Biogeochem. Cycles*, *21*, GB2016 PB–. doi: 10.1029/2006GB002714

Liu, L., & Huang, R. (2012). The global subduction/obduction rates: Their interannual and decadal variability. *Journal of Climate*, *25*, 1096–1115. doi: 10.1175/2011JCLI4228.1

Losch, M., Menemenlis, D., Campin, J.-M., Heimbach, P., & Hill, C. (2010). On the formulation of sea-ice models. Part 1: Effects of different solver implementations and parameterizations. *Ocean Modelling*, *33*(1-2), 129–144. doi: 10.1016/j.ocemod.2009.12.008

Lovenduski, N., & Ito, T. (2009). The future evolution of the Southern Ocean CO2 sink. *Journal of Marine Research*, *67*, 597–617.

Lumpkin, R., & Speer, K. (2007). Global ocean meridional overturning. *Journal of Physical Oceanography*, *37*, 2550–2562. doi: 10.1175/JPO3130.1

Luyten, J., Pedlosky, J., & Stommel, H. (1983). The ventilated thermocline. *Journal of Physical Oceanography*, *13*(2), 292–309.

Marotzke, J., Giering, R., Zhang, K. Q., Stammer, D., Hill, C., & Lee, T. (1999). Construction of the adjoint MIT ocean general circulation model and application to Atlantic heat transport sensitivity. *Journal of Geophysical Research: Atmospheres*, *104*(C12), 29529–29547. doi: 10.1029/1999JC900236

Marshall, J., & Speer, K. (2012). Closure of the meridional overturning circulation through Southern Ocean upwelling. *Nature Geoscience*, *5*(3), 171–180. doi: 10.1038/ngeo1391

Mazloff, M., Heimbach, P., & Wunsch, C. (2010). An Eddy-Permitting Southern Ocean State Estimate. *Journal of Physical Oceanography*, *40*, 880–899.

McDougall, T., & Barker, P. (2011). Getting started with TEOS-10 and the Gibbs Seawater (GSW) Oceanographic Toolbox. *SCOR/IAPSO WG127*.

Meijers, A. J. S. (2013). The Southern Ocean in CMIP5. *Proceedings of the Royal Society A*, 1–21.

Morrison, A., Hogg, A., & Ward, M. L. (2011). Sensitivity of the Southern Ocean overturning circulation to surface buoyancy forcing. *Geophysical Research Letters*, *38*(L14602). doi: 10.1029/2011GL048031

Musgrave, D. (1990). Numerical studies of tritium and helium-3 in the thermocline. *Journal of Physical Oceanography*, *20*, 344–373.

Primeau, F., & Holzer, M. (2006). The Ocean's Memory of the Atmosphere: Residence-Time and Ventilation-Rate Distributions of Water Masses. *Journal of Physical Oceanography*, *36*, 1439–1456.

Roemmich, D., Church, J., Gilson, J., Monselesan, D., Sutton, P., & Wijffels, S. (2015). Unabated planetary warming and its ocean structure since 2006. *Nature Publishing Group*, *5*(3), 240. doi: 10.1038/nclimate2513

Russell, J., Dixon, K., Gnanadesikan, A., Stouffer, R., & Toggweiler, J. (2006). The Southern Hemisphere westerlies in a warming world: Propping open the door to the deep ocean. *Journal of Climate*, *19*, 6382–6390.

Sabine, C., Feely, R., Gruber, N., Key, R., Lee, K., Bullister, J. L., … Rios, A. F.

(2004). The oceanic sink for anthropogenic CO2. *Science*, *305*(367). doi: 10.1126/science.1097403

Sallée, J., & Rintoul, S. (2011). Parameterization of eddy-induced subduction in the Southern Ocean surface-layer. *Ocean Modelling*, *39*, 146–153.

Sallée, J., Speer, K., Rintoul, S., & Wijffels, S. (2010). Southern Ocean thermocline ventilation. *Journal of Physical Oceanography*, *40*, 509–529.

Sallée, J.-B., Matear, R. J., Rintoul, S. R., & Lenton, A. (2012). Localized subduction of anthropogenic carbon dioxide in the Southern Hemisphere oceans. *Nature Geoscience*, *5*(8), 579–584. doi: 10.1038/ngeo1523

Sallée, J.-B., Speer, K., Rintoul, S., & Wijffels, S. (2010). Southern Ocean Thermocline Ventilation. *Journal of Physical Oceanography*, *40*(3), 509–529. doi: 10.1175/2009jpo4291.1

Sarmiento, J. L., Gruber, N., Brzezinski, M. A., & Dunne, J. P. (2004). High-latitude controls of thermocline nutrients and low latitude biological productivity. *Nature*, *427*(6969), 56–60. doi: 10.1038/nature02127

Sévellec, F., & Fedorov, A. V. (2015). Optimal excitation of AMOC decadal variability: Links to the subpolar ocean. *Progress in Oceanography*, *132*, 287–304. doi: 10.1016/j.pocean.2014.02.006

Speer, K., & Forget, G. (2013). Global Distribution and Formation of Mode Waters. In *Ocean circulation and climate - a 21st century perspective* (pp. 211–226). Elsevier. doi: 10.1016/B978-0-12-391851-2.00009-X

Speer, K., Rintoul, S., & Sloyan, B. (2000). The Diabatic Deacon Cell. *Journal of Physical Oceanography*, *30*(12), 3212–3222.

Speer, K., & Tziperman, E. (1992). Rates of water mass formation in the North Atlantic Ocean. *Journal of Physical Oceanography*, *22*, 93–104.

Talley, L. (2008). Freshwater transport estimates and the global overturning circulation: Shallow, deep and throughflow components. *Progress in Oceanography*, *78*(3), 257–303. doi: 10.1016/j.pocean.2008.05.001

Talley, L. (2013). Closure of the Global Overturning Circulation Through the Indian, Pacific, and Southern Oceans: Schematics and Transports. *Oceanography*, *26*(1), 80–97. doi: 10.5670/oceanog.2013.07

Thacker, W. C., & Long, R. B. (1988). Fitting dynamics to data. *Journal of Geophysical Research*, *93*(C2), 1227–1240. doi: 10.1029/JC093iC02p01227

Trossman, D. S., Thompson, L., Mecking, S., & Warner, M. J. (2012). On the formation, ventilation, and erosion of mode waters in the North Atlantic and Southern Oceans. *Journal of Geophysical Research - Oceans*, *117*. doi: 10.1029/2012JC008090

Verdy, A., Mazloff, M. R., Cornuelle, B. D., & Kim, S. Y. (2014). Wind-Driven Sea Level Variability on the California Coast: An Adjoint Sensitivity Analysis. *Journal of Physical Oceanography*, *44*(1), 297–318. doi: 10.1175/JPO-D-13-018.1